

# Sound emission and annihilations in a programmable quantum vortex collider

Accepted: 22 September 2021

W. J. Kwon<sup>1,2</sup>✉, G. Del Pace<sup>1,2</sup>, K. Khani<sup>1,2</sup>, L. Galantucci<sup>3</sup>, A. Muzi Falconi<sup>1,2</sup>, M. Inguscio<sup>1,2,4</sup>, F. Scazza<sup>1,2,5</sup> & G. Roati<sup>1,2</sup>

In quantum fluids, the quantization of circulation forbids the diffusion of a vortex swirling flow seen in classical viscous fluids. Yet, accelerating quantum vortices may lose their energy into acoustic radiations<sup>1,2</sup>, similar to the way electric charges decelerate on emitting photons. The dissipation of vortex energy underlies central problems in quantum hydrodynamics<sup>3</sup>, such as the decay of quantum turbulence, highly relevant to systems as varied as neutron stars, superfluid helium and atomic condensates<sup>4,5</sup>. A deep understanding of the elementary mechanisms behind irreversible vortex dynamics has been a goal for decades<sup>3,6</sup>, but it is complicated by the shortage of conclusive experimental signatures<sup>7</sup>. Here we address this challenge by realizing a programmable vortex collider in a planar, homogeneous atomic Fermi superfluid with tunable inter-particle interactions. We create on-demand vortex configurations and monitor their evolution, taking advantage of the accessible time and length scales of ultracold Fermi gases<sup>8,9</sup>. Engineering collisions within and between vortex–antivortex pairs allows us to decouple relaxation of the vortex energy due to sound emission and that due to interactions with normal fluid (that is, mutual friction). We directly visualize how the annihilation of vortex dipoles radiates a sound pulse. Further, our few-vortex experiments extending across different superfluid regimes reveal non-universal dissipative dynamics, suggesting that fermionic quasiparticles localized inside the vortex core contribute significantly to dissipation, thereby opening the route to exploring new pathways for quantum turbulence decay, vortex by vortex.

Quantized vortices are a ubiquitous form of topological excitation in quantum matter. Their motion governs the resistive behaviour of superconductors<sup>10,11</sup>, as well as the emergence of many dissipative collective phenomena in superfluids, ranging from vortex lattices to the quantum turbulence of chaotic vortex tangles<sup>3</sup>. In any quantum fluid, the superflow circulation around a vortex can take only discrete values, making vorticity intrinsically robust. However, travelling vortices interact with the normal component and experience mutual friction<sup>12</sup>, which causes dissipation of the superflow. Even in the absence of a normal fluid, it has been proposed that vortex–sound interactions may lead to the transformation of kinetic energy associated with the superflow around vortices (incompressible) into kinetic energy associated with sound waves (compressible), providing the ultimate mechanism behind the decay of quantum turbulence<sup>13–15</sup>. In three-dimensional (3D) vortices, the emission of sound waves is triggered by the accelerated motion of vortex lines at sufficiently short scales, resulting from vortex reconnections<sup>16–18</sup> and helical Kelvin-wave cascades<sup>14,15,19–21</sup>. Similarly, accelerating 2D point vortices may dissipate energy by emitting sound waves, much like an accelerated electric charge radiates electromagnetic waves<sup>1</sup>. In this analogy, which becomes apparent by considering the mathematical

description of the 2D Bose superfluid and (2 + 1)D electrodynamics, vortices and phonons play the roles of electric charges and photons, respectively<sup>22–24</sup>.

Despite prolonged efforts in superfluid helium<sup>25,26</sup>, sound-mediated dissipation of vortex energy remains elusive due to the scarcity of convincing experimental proofs<sup>7,27</sup>. Another central question is how vortex–sound interactions could be influenced by the fermionic or bosonic nature of superfluids<sup>4</sup>. In fermionic superfluids, pair-breaking excitations become energetically accessible, and vortices have intricate structures filled up with quasiparticle bound states even at zero temperature<sup>28–31</sup>. Such fermionic states are thought to provide an additional dissipation sink by absorbing the vortex energy<sup>32</sup>, which may in turn compete with dissipation via phonon emission<sup>4</sup>. This is in stark contrast to weakly interacting bosonic superfluids, where the empty vortex core is directly connected to the vanishing order parameter.

In this work, we study the fundamental mechanisms of vortex energy dissipation by realizing a versatile 2D vortex collider in homogeneous atomic superfluids. We unveil the coupling between vortex and sound by observing the conversion of the energy of vortex swirling flow into sound energy during vortex collisions. We visualize

<sup>1</sup>European Laboratory for Nonlinear Spectroscopy (LENs), Sesto Fiorentino, Italy. <sup>2</sup>Istituto Nazionale di Ottica del Consiglio Nazionale delle Ricerche (CNR-INO), Sesto Fiorentino, Italy. <sup>3</sup>Joint Quantum Centre (JQC) Durham–Newcastle, School of Mathematics, Statistics and Physics, Newcastle University, Newcastle upon Tyne, UK. <sup>4</sup>Department of Engineering, Campus Bio-Medico University of Rome, Rome, Italy. <sup>5</sup>Present address: Department of Physics, University of Trieste, Trieste, Italy. ✉e-mail: kwon@lens.unifi.it

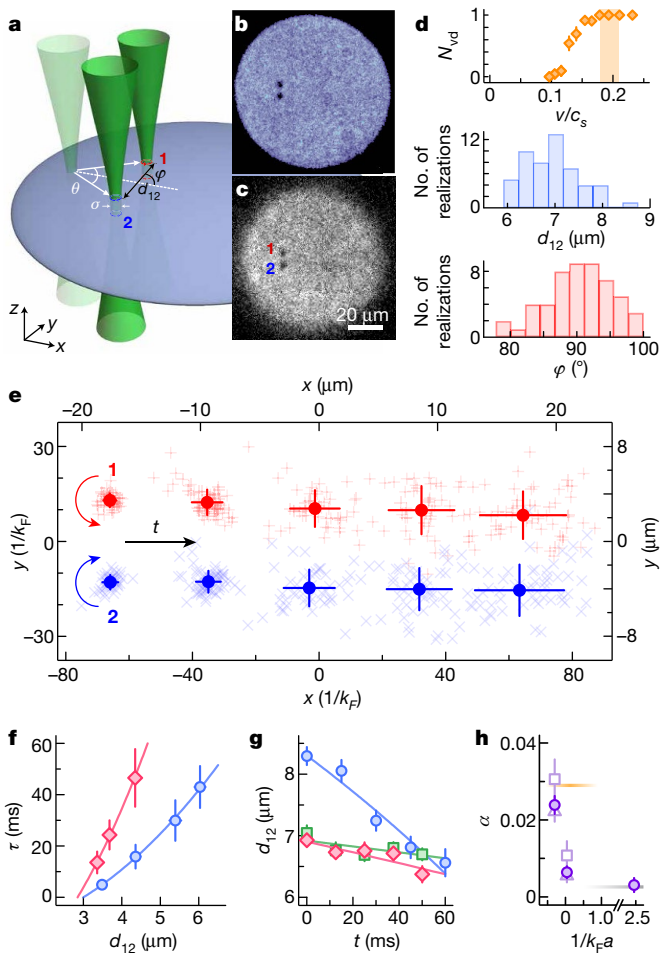


**Fig. 1 | Deterministic generation and frictional dissipation of single vortex dipoles.** **a**, The dipole generation protocol: we move two obstacles by  $10\ \mu\text{m}$  with velocity  $v$  and relative angle  $\theta$  through a thin, homogeneous superfluid, pinning a vortex-antivortex pair. **b**, In situ image of the UFG sample with obstacles in their final positions. **c**, TOF image (Methods) of the UFG, averaged over three experimental realizations, acquired after the obstacles have been removed, revealing a single vortex-antivortex pair. **d**, Properties of generated vortex dipoles in UFGs for  $\theta \approx 20^\circ$ : mean dipole number  $N_{\text{vd}}$  (top), inter-vortex separation  $d_{12}$  (middle) and direction  $\varphi$  (bottom). The histograms are obtained with  $v/c_s \approx 0.2$  and obstacle height  $V_0/\mu \approx 2.2$ , where  $c_s$  is the sound speed and  $\mu$  is the pair chemical potential. **e**, Trajectory of single dipoles in UFGs, prepared with  $d_{12} = 6.9(6)\ \mu\text{m}$  and  $\varphi = 90(5)^\circ$  (see **d**). Data are collected for hold times  $0 \leq t \leq 50$  ms in steps of  $12.5$  ms. Light red plus (blue cross) signs represent the distribution of vortices (antivortices) detected at each time  $t$ , while red (blue) circles depict their positions averaged over  $\sim 40$  experimental runs. Here,  $1/k_F = 0.27(1)\ \mu\text{m}$ . **f**, Short dipole half-lifetime  $\tau$  measured in BCS (blue circles) and UFG (red diamonds) samples. **g**, Time evolution of  $d_{12}$  in BCS (blue circles), UFG (red diamonds) and BEC (green squares) samples. Solid lines in **f** and **g** are fits with a DPV model (Methods). **h**, Mutual friction coefficient  $\alpha$  across the BEC-BCS crossover. Violet circles denote the weighted mean value of  $\alpha$  extracted from **f** (light squares) and **g** (light triangles). The grey and orange horizontal lines denote the values of  $\alpha$  obtained in ref. <sup>46</sup> for a weakly interacting BEC at  $T = 0.3T_c$ , and in ref. <sup>48</sup> for a strongly interacting, 2D holographic superfluid at  $T = 0.45T_c$ , respectively. Error bars of **d** and **g** indicate the standard error of the mean (Methods), while they represent the standard deviation for **e**, and standard fitting errors for **f** and **h**.

vortices annihilating into sound waves (that is, the ultimate outcome of small-scale four-vortex collisions), and find good agreement with theoretical simulations, shedding light on such fundamental process<sup>33–35</sup>. Tuning our system away from the bosonic regime into a superfluid of weakly bound fermion pairs, we observe a considerable increase of

mutual friction as well as the breakdown of a low-temperature picture essentially based on sound-mediated dissipation, hinting at the importance of vortex-core-bound fermionic excitations. For our studies, we follow a bottom-up approach reminiscent of other atomic platforms featuring control at the single-particle level, and gain exquisite control of individual 2D vortices to assemble them one by one in arbitrary arrangements. Such controllable 2D vortex systems, where vortex-line excitations have only a moderate role<sup>36</sup>, allow us to efficiently track vortex trajectories and hunt for visual evidence of low-energy acoustic radiation. The building blocks of our collider are vortex dipoles, namely self-propelling vortex-antivortex pairs carrying a constant linear fluid momentum, previously observed in both bosonic<sup>37</sup> and fermionic<sup>38</sup> atomic superfluids. Tracking a dipole is ideal for probing the thermal friction, under whose action it gradually shrinks in size and eventually self-annihilates. Injecting another dipole triggers a dipole-dipole collision<sup>17</sup>, providing a minimalistic yet effective way to promote vortex acceleration, favouring in turn energy dissipation. Thereby, we progress towards a complete microscopic description of the dissipative dynamics of both single and colliding vortex-antivortex pairs, which is at the heart of the relaxation of nonequilibrium states in bosonic and fermionic superfluids<sup>3,5,7–9</sup>.

Our experiment starts with thin, uniform superfluids of paired fermionic <sup>6</sup>Li atoms trapped inside a circular box of  $45\ \mu\text{m}$  radius (Fig. 1a, b) at a temperature  $T = 0.3(1)T_c$ , where  $T_c$  is the critical temperature of the superfluid transition. Tuning the *s*-wave scattering length  $a$  between two different atomic states, we access three different coupling regimes, namely a Bardeen-Cooper-Schrieffer superfluid of fermionic pairs (BCS,  $1/k_F a \approx -0.31$ ), a unitary Fermi gas (UFG,  $1/k_F a \approx 0.04$ ) and a Bose-Einstein condensate of tightly bound molecules (BEC,  $1/k_F a \approx 2.5$ ). Here,  $k_F = (6\pi^2 n)^{1/3}$  is the Fermi wavevector, estimated from the central density  $n$  along the *z* axis. To deterministically create a dipole in a desired position and propagation direction, we implement the so-called chopstick method<sup>39</sup> (Fig. 1a). We split an initial Gaussian repulsive obstacle of  $1/e^2$  width  $\sigma = 1.3(1)\ \mu\text{m}$  into two and simultaneously move them with velocity  $v$  obliquely at a tuning angle  $\theta$  (Methods). When  $v$  exceeds a critical value, a single dipole is created and pinned around the obstacles (Fig. 1b, c) with near-unit probability, reproducible size  $d_{12}$  and direction  $\varphi$  (Fig. 1d), resulting in well-defined single-dipole trajectories (Fig. 1e). We control  $d_{12}$  by adjusting  $\theta$ , accessing small length scales down to  $d_{12} \lesssim 3\ \mu\text{m}$ , which is a few times the vortex core radius  $\xi_v$ . Given the homogeneity of the sample (Extended Data Fig. 2), we can fully characterize vortex energy dissipation with the single parameter  $d_{12}$ , linked to both the incompressible kinetic energy of the superflow  $E \propto \log(d_{12}/\xi_v)$  and the linear fluid momentum  $P \propto d_{12}$  carried by a dipole<sup>40</sup>. Such expressions are reasonably accurate at the experimentally explored  $d_{12}$  larger than a few  $\xi_v$ , while they are expected to fail at very small  $d_{12}$  (ref. <sup>41</sup>). We verify that vortex-dipole speed is  $\propto 1/d_{12}$ , such that faster dipoles have lower  $P$  and  $E$ .

We first conduct single-dipole experiments, observing a tapering of trajectories over the propagation time  $t$ . The decrease of  $d_{12}(t)$  reflects the effective attraction between vortex and antivortex arising from mutual friction. This causes dipoles to shrink down to a critical size  $d_c$  before self-annihilating, possibly before reaching the boundary of the cloud. We extract the dipole half-lifetime  $\tau$  as a function of initial  $d_{12}$  in UFG and BCS regimes, by measuring the evolution of the mean dipole number  $N_{\text{vd}}(t)$  (Fig. 1f, raw data in Extended Data Fig. 3). Data are fitted with a dissipative point-vortex (DPV) model<sup>12</sup> (Fig. 1f, g solid lines, Methods), which accounts for the interaction of thermal excitations in the bulk with a vortex, allowing us to extract the mutual friction coefficient  $\alpha$  at a given temperature. From the *x* intercept of the fitting curves, we obtain  $d_c \approx 10/k_F \approx 10\xi_v$  in both regimes, where  $\xi_v \approx 1/k_F$  (refs. <sup>31,42–44</sup>). Conversely, in bosonic superfluids we do not observe single-dipole self-annihilations, even for  $d_{12} \approx 5\xi$ , where  $\xi = 0.68(2)\ \mu\text{m}$  is the BEC healing length with  $\xi \approx \xi_v$  (Extended Data Fig. 1). This is consistent with predicted  $d_c \sim 2\xi$  (refs. <sup>17,45</sup>). Such deviating  $d_c$  could stem from the

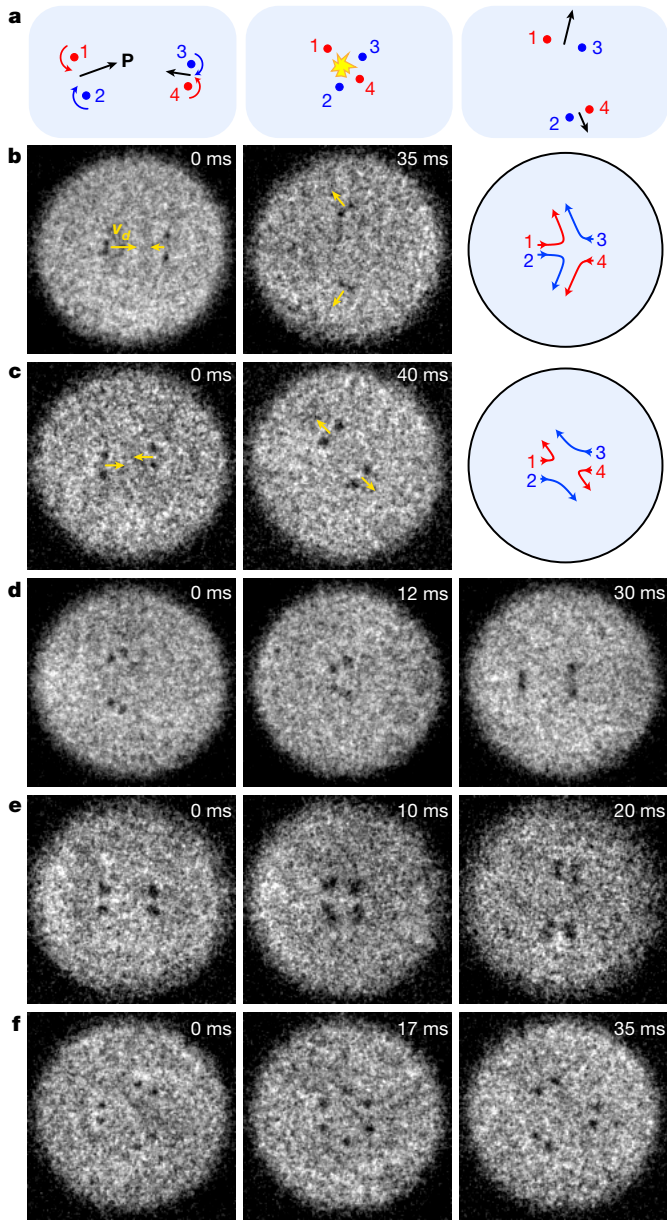


**Fig. 2 | Arbitrary vortex collisions on demand.** **a**, The collision between two dipoles ('12' and '34'), during which new pairs ('13' and '24') are formed, and move away with new momenta. **b, c**, Collisions between two dipoles with different sizes (**b**) and between two dipoles with similar sizes and an impact parameter  $b \approx 0.5d_{12}$  (**c**). The right-most panels show the expected trajectories, calculated with the DPV model. Arrows in **a** denote the momentum vectors of each dipole, while in **b, c** they represent the dipole velocity. **d**, Oblique collision of two dipoles under a  $120^\circ$  angle: the resulting dynamics is close to time-reversing that in **b**. **e**, Head-on collision of two doubly charged dipoles in UFGs. **f**, Symmetric collision of three dipoles. All images are recorded in molecular BECs, except for **e**, at hold times  $t$  noted on top of each panel. Images shown are either averaged over two repeated experimental runs (**b** left and **d**) or single shots.

complicated vortex core structures and weaker pairing strength of fermionic (UFG and BCS) superfluids. Nonetheless, we cannot exclude effects of a relatively larger thickness along the  $z$  direction in these regimes (Methods), which might allow effectively  $\sim 6$  times longer vortex lines to bend and increase  $d_c$ .

To gain further insight into mutual friction, we monitor the  $d_{12}(t)$  evolution for  $d_{12} > d_c$  in all superfluid regimes (Fig. 1g). We fit data with the DPV model, and the extracted  $\alpha$  from  $d_{12}(t)$  and lifetime measurements

are summarized in Fig. 1h. As signalled by the shorter  $\tau$  and the steeper drop of  $d_{12}(t)$ ,  $\alpha$  is found to sharply increase when crossing to the BCS regime, whereas it slowly decreases when going from unitarity to a BEC. This does not appear compatible with the mere scattering of normal excitations in the bulk by the moving vortices, as the normal fractions are comparably small in all three regimes at similarly low temperature  $T = 0.3(1)T_c$ . Instead, this may indicate that the complex vortex core structure of fermionic superfluids, filled with unpaired bound levels<sup>29–31</sup> (that is, Andreev bound states), affects the mutual friction by interacting with bulk normal excitations<sup>29</sup>. Indeed, the rise of  $\alpha$  from the UFG to the BCS regime could be explained by the proliferation of bound quasiparticles in the latter<sup>31</sup>. On the other hand, the small value of  $\alpha$  measured in our finite-temperature BEC is found to be in agreement with previous work<sup>46,47</sup>, and signifies a small effect from thermal atoms occupying the vortex core. We also compare our findings at strong coupling with a recent theoretical prediction  $\alpha = 0.029$  based on 2D holographic superfluids at  $T/T_c = 0.45$  (ref. 48), higher than  $\alpha \approx 0.006$  measured at unitarity, deserving further investigations. Measuring the temperature dependence of  $\alpha$  throughout the BEC–BCS crossover will deepen our understanding of mutual friction mechanisms and provide a benchmark for theories of strongly interacting fermionic superfluids.

Scaling up our single-dipole control, we engineer and demonstrate various paradigmatic vortex collisions<sup>49</sup> (Fig. 2), serving as the starting point to investigate dissipation in binary dipole collisions (Fig. 2a). We can perform dipole–dipole collisions with controllable dipole sizes (Fig. 2b), impact parameter  $b$  (Fig. 2c) and scattering angle (Fig. 2d). When dissipation effects are negligible and  $d_{12}, d_{34} \gg d_c$ , the collision dynamics is fully explained by momentum and energy conservation. Together with  $b$ , this determines the scattering angles observed in Fig. 2b, c. This is evident in Fig. 2d, where a time-reversed version of Fig. 2b is realized. Further, we extend our deterministic generation to produce doubly charged dipoles in a UFG (Methods), and investigate their head-on collisions (Fig. 2e). During its propagation, each doubly charged vortex splits into a pair of same-circulation vortices due to dynamical instability, forming a charge-2 cluster (Fig. 2e,  $t = 10$  ms). Finally, we exemplify the scalability of our collider by demonstrating a symmetric six-vortex collision (Fig. 2f). Although the input and output configurations do not necessarily entail a collision, the exchange of partners between dipoles becomes clear from the hexagonal pattern observed at intermediate time. Figure 2 demonstrates programmable manipulation of vortex configurations on demand.

We now focus on the regime of strong dissipation driven by high vortex accelerations within a collision. We study head-on collisions between two symmetric dipoles by varying their initial sizes  $d_{12}$  and  $d_{34}$  with  $b \approx 0$  and  $\langle d_{12} \rangle \approx \langle d_{34} \rangle$ . To enhance the acceleration effect for given initial vortex energy, we also realize oblique collisions at  $120^\circ$  (as in Fig. 2d). In both cases, each dipole is created at a distance  $L$  from the cloud centre, where  $12.5 \mu\text{m} \lesssim L \lesssim 14 \mu\text{m}$  (Fig. 3a, BECs). Figure 3b shows the head-on collision trajectory observed in a BCS superfluid on setting  $d_{12} \approx d_{34}$  to be similar to that of Fig. 3a. In comparison with the bosonic regime, the exiting dipoles have significantly shrunk, signalling that much stronger dissipation occurs in BCS superfluids. We quantify the energy loss during a collision by measuring the dipole sizes in the initial and final configurations, when the inter-dipole distance is around  $2L$ . The ratio between final and initial dipole sizes,  $\Gamma \equiv d_{12}d_{24}/d_{12}d_{34}$ , directly reflects the change in the kinetic energy of the swirling flow  $\Delta E$  caused by the collision. Indeed, the energy of two far-apart dipoles is well approximated by  $E \propto \log(d_{12}/\xi_v) + \log(d_{34}/\xi_v)$ ; hence,  $\Delta E \propto \log(d_{12}d_{24}/d_{12}d_{34})$ . The measured values of  $\Gamma$  are displayed in Fig. 3c–e as a function of  $d_{in} \equiv \sqrt{\langle d_{12}d_{34} \rangle}$ , exhibiting a clear decreasing trend while reducing  $d_{in}$  in all superfluid regimes. We compare them with predictions of the DPV model (dotted lines, head-on) obtained by inserting the measured  $\alpha$  (Fig. 1h). Whereas for the largest explored  $d_{in}$ , where  $\Gamma \gtrsim 0.9$  in each regime, mutual friction seems sufficient to account for the observed behaviour, the pronounced drop of  $\Gamma$  for smaller  $d_{in}$  reveals that other non-thermal sources of

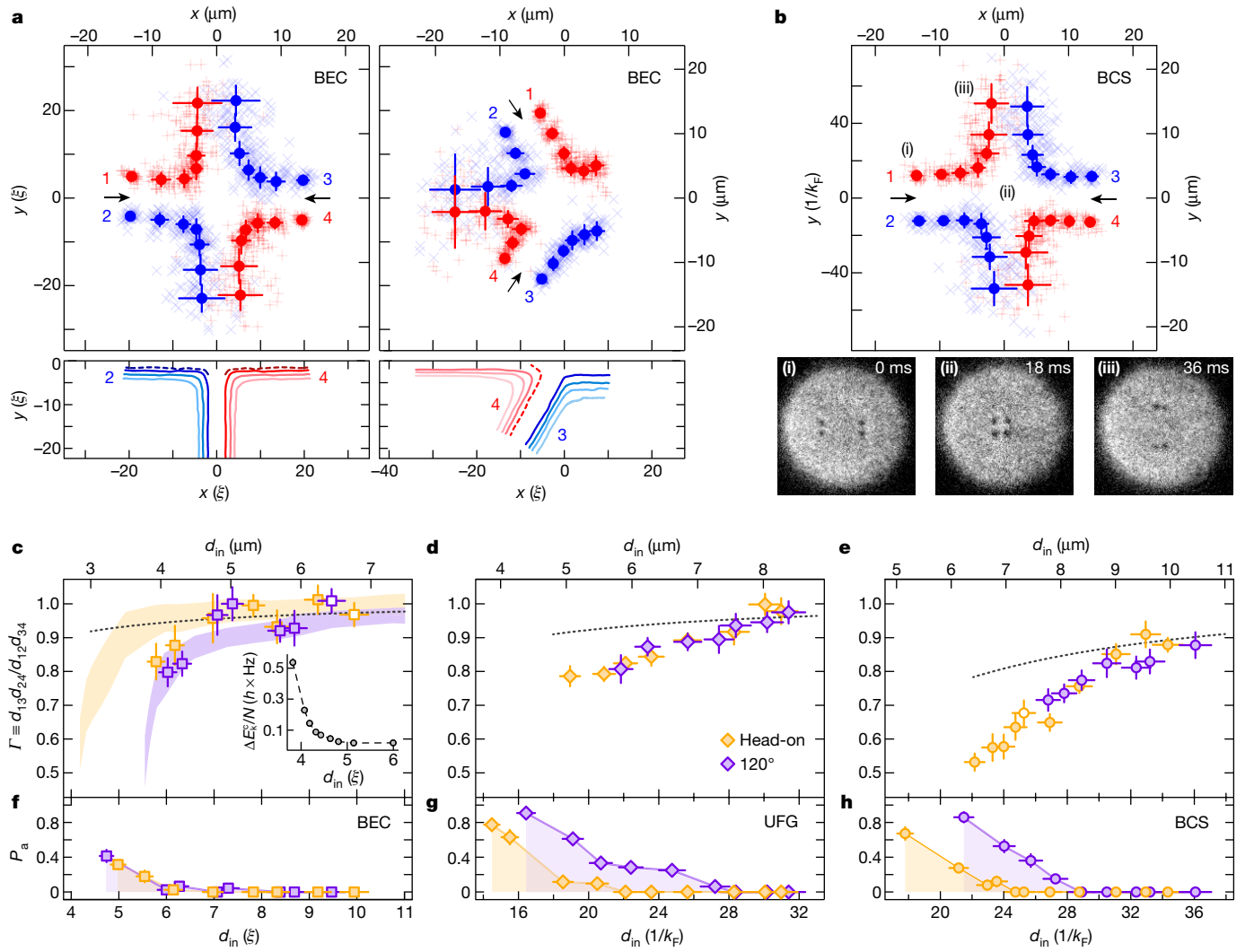


**Fig. 3 | Dissipation and annihilation in two-dipole collisions.**

**a**, Experimental trajectories of head-on (left) and  $120^\circ$  (right) collisions in BECs. Transparent cross and plus signs indicate the vortex-antivortex positions in single experimental realizations, while full circles denote the averages over repeated experiments. The bottom panels show GPE-simulated trajectories for various  $d_{in}$ . Same colours denote equal  $d_{in}$ , while dashed lines denote the annihilating trajectories. **b**, Top, experimental trajectory of head-on collision in a BCS superfluid, setting  $d_{in}$  similar to that of **a**. Bottom, vortex images averaged over a few experimental shots are shown for three evolution times (i)–(iii) within the trajectory. All experimental trajectories are obtained by  $\sim 40$  realizations for each  $t$  with the time interval 6 ms.

**c–h**,  $\Gamma \equiv d_{13}d_{24}/d_{12}d_{34}$  and annihilation probability  $P_a$  measured for various  $d_{in}$  in the different superfluid regimes. Orange (purple) symbols denote the experimental values obtained from head-on ( $120^\circ$ ) collisions. Open symbols in **c** and **e** mark the experiments shown in **a** and **b**, respectively. Shaded bands and black dotted lines correspond to the predicted values of  $\Gamma$  from GPE simulations and DPV model solutions, respectively (Methods). The inset of **c** shows the GPE-computed change of compressible kinetic energy  $\Delta E_k^c/N$  throughout a head-on collision as a function of  $d_{in}$  (points and a connecting dashed line), where  $N$  is the total number of pairs. Error bars for **c–h** indicate the standard errors of the mean over 30–100 realizations, while they represent the standard deviation of measurements for **a** and **b**.

dissipation kick in. As the finite compressibility of our superfluid can become important when vortices start overlapping, we expect the enhanced incompressible kinetic energy loss at short  $d_{in}$  to be associated with sound-like density excitations.

We compare our measurements in the BEC regime with Gross-Pitaevskii equation (GPE) simulation results. From numerical trajectories (as in Fig. 3a), we extract the trends of  $\Gamma$  (Methods) and plot them in Fig. 3c as shaded bands. We find clear monotonic behaviours for both head-on and  $120^\circ$  collisions, matching the observed reduction of  $\Gamma$  for small  $d_{in}$ . We compute also the compressible kinetic energy variation  $\Delta E_k^c$  throughout the head-on collision (Fig. 3c, inset), which evidences how part of the incompressible kinetic energy is indeed converted to compressible sound energy. To elucidate the origin of the sharp decrease of  $\Gamma$ , it is instructive to estimate the acoustic energy radiated by an accelerating vortex in analogy with the Larmor formula

for the power radiated by an accelerating charge. Assuming symmetric head-on collisions and negligible vortex cores, this gives approximately  $\Delta E_k^c \propto 1/d_{in}^4$  (ref. 17). This qualitatively explains the steep behaviour observed in the BEC regime and illustrates the role of vortex acceleration in phonon emission. The larger dissipation in oblique collisions seems consistent with the larger acceleration sustained in this case. On the contrary, the vortex energy dissipated throughout head-on and oblique collisions appears gradual both in UFG and BCS regimes, being stronger in the latter case. Within a point-vortex model, where vortex motions are determined by their positions, vortex acceleration depends only on  $d_{in}$ . This should apply whenever  $d_{in} \gg \xi_v$ . Thus, the deviating  $\Gamma$  measured in the various superfluids signals that acceleration couples to distinct dissipation mechanisms in each regime, adding to the emission of phononic quasiparticles. One predicted scenario is the emission of fermionic quasiparticles

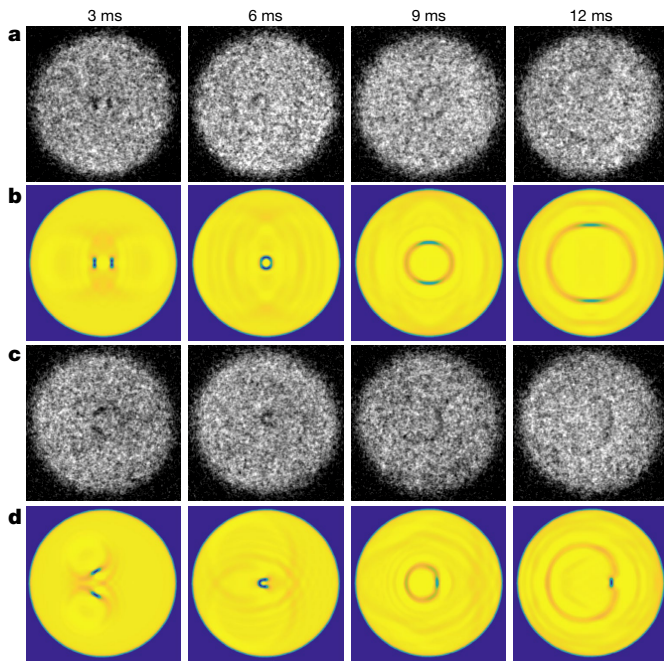


**Fig. 4 | Direct observation of the sound emission from dipole-dipole annihilation events.** **a, c,** Experimental images of annihilation dynamics for head-on (**a**) and  $120^\circ$  (**c**) collisions, recorded in BEC superfluids for  $d_{in} < 5\xi$ . **b, d,** GPE-simulated images (central  $x$ - $y$  plane of the cloud) of the annihilation processes for a head-on collision with  $d_{in} = 2.9\xi$  (**b**) and a  $120^\circ$  collision with  $d_{in} = 2.6\xi$  (**d**). Each experimental image is obtained from an independent experimental run.

from the vortex cores, as a consequence of the local heating of accelerating vortices<sup>32</sup>, providing a possible explanation for the stronger dissipation observed in BCS superfluids.

Dipole-dipole collisions offer also a unique opportunity to systematically investigate vortex annihilation. Away from the strong-friction limit, where the single-dipole self-annihilation can prevail even in the relaxation of superfluid turbulence<sup>33,35,50–52</sup>, annihilation is essentially a many-vortex (four-vortex-dominant) process<sup>51–54</sup>. We determine the annihilation probability  $P_a$  by counting the fraction of annihilation events, shown in Fig. 3f–h as a function of  $d_{in}$ . We estimate the critical initial size  $d_a$  for annihilation, such that  $P_a(d_{in} \leq d_a) \geq 0.5$ , obtaining for head-on collisions  $d_a \approx 4\xi$  in the BEC,  $d_a \approx 16/k_f$  in the UFG and  $d_a \approx 19/k_f$  in the BCS regime. In  $120^\circ$  collisions, we mostly observe partial annihilation of the shorter outgoing dipole (Extended Data Fig. 4), occurring at  $d_a \sim 30\%$  larger than the head-on case, because of the final asymmetric configuration<sup>55</sup>. The extracted  $\Gamma$  and  $d_a$  suggest that annihilation occurs whenever the energy dissipated during the collision is sufficiently large to reduce the dipole size to about  $d_c$  (ref. 17). Here we exclude that self-annihilations are significant by inspecting  $N_{vd}(t)$  (Extended Data Fig. 4).

Annihilation is the most dramatic consequence of vortex-sound interaction, converting both vortex core and incompressible kinetic energies into compressible sound energy. We directly visualize the sound emission from dipole-dipole annihilation events both in head-on (Fig. 4a) and  $120^\circ$  (Fig. 4c) collisions. In the first case, the vortices coalesce shortly after the collision and soon they are converted into a circular density depletion propagating outwards. We analyse the wavefronts of the outgoing pulses and confirm that their speed matches the expected sound speed, supporting the acoustic nature of the excitation (Extended Data Fig. 5). In  $120^\circ$  collisions, it is difficult to detect sound emission from the partial annihilation of the shorter dipole, due to its small energy. Despite their very low occurrence probability, complete annihilations are also observed (Fig. 4c), where the

high-amplitude density pulse travelling rightward is radiated from the annihilation of the longer dipole. GPE results (Fig. 4b, d) are consistent with experimental observations. Interestingly, we numerically confirm that the density wave created by the head-on collision is not circularly symmetric, as the rarefaction pulse<sup>45</sup> generated shortly after the annihilation propagates along the  $y$  axis, and eventually decays into sound (Fig. 4b). Moreover, in  $120^\circ$  collisions (Fig. 4d), the right-moving dipole does not seem to annihilate permanently, but revives as a U-shaped vortex line with handles ending at the boundary of the condensate. Such low-energy vortex-handle excitations appearing in regions of small density are expected to be fragile, and thus hardly observable at finite temperatures as in our experiment. On the other hand, in BCS and UFG superfluids, clear acoustic waves from vortex annihilations are observed rarely (Extended Data Figs. 4 and 5). This could be associated with the higher speed of sound  $c_s$  in these regimes, resulting in low-amplitude density waves as  $v_p/c_s = \delta n/n_0$ , where  $v_p$  is the local velocity of atom pairs, and  $\delta n$  is the amplitude of the excitation for the density  $n_0$ . Nonetheless, other possibilities unique to these regimes can be envisioned, such as the total delocalization of fermionic quasiparticles originally bound in the vortex cores, which may affect sound emission. Our observations are in line with the distinct trends of  $\Gamma$ , supporting that vortex-sound interactions are not the only relevant dissipation mechanism throughout vortex collisions.

In conclusion, building a novel platform for 2D vortex collisions in atomic Fermi superfluids, we provide a comprehensive picture of vortex decay arising from mutual friction and vortex-sound interaction, connecting to experiments in superfluid  $^3\text{He}$  and  $^4\text{He}$  (ref. 7). We visualize vortex annihilation events, providing direct evidence of the ensuing sound emission. In BECs, we link the vortex energy dissipated into phononic excitations with the acceleration in dipole-dipole collisions, supporting the close relationship between superfluid 2D vortex dynamics and electrohydrodynamics. On the other hand, our observations in BCS and unitary superfluids defy a description based solely on thermal friction and sound emission, pointing to additional contributions from fermionic quasiparticles localized in vortex cores, and from their emission by accelerating vortices. This poses a compelling question about the universal and non-universal aspects of irreversible vortex dynamics across the BEC-BCS crossover<sup>56</sup>. Extending our work towards 2D quantum turbulence<sup>3,34,35,57–62</sup>, we could study the collisions of clusters, which may further substantiate the specific roles of vortex acceleration in vortex-sound interaction. Another future direction is to investigate vortex-sound interactions from a reversed perspective, letting vortices absorb sound energy<sup>1</sup>. The capability of producing programmable vortex configurations in tunable superfluids opens new horizons for vortex research (for example, in lower-dimensional quasi-condensates)<sup>54</sup>. Combined with optical disorder potentials, this may contribute to the quest for high-performance superconductors by examining exotic phases of vortex matter.

## Online content

Any methods, additional references, Nature Research reporting summaries, source data, extended data, supplementary information, acknowledgements, peer review information; details of author contributions and competing interests; and statements of data and code availability are available at <https://doi.org/10.1038/s41586-021-04047-4>.

- Parker, N. G., Proukakis, N. P., Barenghi, C. F. & Adams, C. S. Controlled vortex-sound interactions in atomic Bose-Einstein condensates. *Phys. Rev. Lett.* **92**, 160403 (2004).
- Barenghi, C. F., Parker, N. G., Proukakis, N. P. & Adams, C. S. Decay of quantised vorticity by sound emission. *J. Low Temp. Phys.* **138**, 629–634 (2005).
- Tsubota, M., Kobayashi, M. & Takeuchi, H. Quantum hydrodynamics. *Phys. Rep.* **522**, 191–238 (2013).
- Vinen, W. F. & Niemela, J. J. Quantum turbulence. *J. Low Temp. Phys.* **128**, 167–231 (2002).
- Barenghi, C. F., Skrbek, L. & Sreenivasan, K. R. Introduction to quantum turbulence. *Proc. Natl Acad. Sci. USA* **111**, 4647–4652 (2014).
- Feynman, R. P. in *Progress in Low Temperature Physics* Vol. 1, 17–53 (Elsevier, 1955).

7. Vinen, W. Quantum turbulence: achievements and challenges. *J. Low Temp. Phys.* **161**, 419–444 (2010).
8. Zwierlein, M. W., Abo-Shaeer, J. R., Schirotzek, A., Schunck, C. H. & Ketterle, W. Vortices and superfluidity in a strongly interacting Fermi gas. *Nature* **435**, 1047–1051 (2005).
9. Ku, M. J. H., Mukherjee, B., Yefsah, T. & Zwierlein, M. W. Cascade of solitonic excitations in a superfluid Fermi gas: from planar solitons to vortex rings and lines. *Phys. Rev. Lett.* **116**, 045304 (2016).
10. Bardeen, J. & Stephen, M. J. Theory of the motion of vortices in superconductors. *Phys. Rev.* **140**, A1197–A1207 (1965).
11. Blatter, G., Feigel'man, M. V., Geshkenbein, V. B., Larkin, A. I. & Vinokur, V. M. Vortices in high-temperature superconductors. *Rev. Mod. Phys.* **66**, 1125–1388 (1994).
12. Hall, H. E. & Vinen, W. F. The rotation of liquid helium II – II. The theory of mutual friction in uniformly rotating helium II. *Proc. R. Soc. Lond. A* **238**, 215–234 (1956).
13. Nore, C., Abid, M. & Brachet, M. E. Kolmogorov turbulence in low-temperature superflows. *Phys. Rev. Lett.* **78**, 3896–3899 (1997).
14. Vinen, W. F. Decay of superfluid turbulence at a very low temperature: the radiation of sound from a Kelvin wave on a quantized vortex. *Phys. Rev. B* **64**, 134520 (2001).
15. Vinen, W. F., Tsubota, M. & Mitani, A. Kelvin-wave cascade on a vortex in superfluid  $^4\text{He}$  at a very low temperature. *Phys. Rev. Lett.* **91**, 135301 (2003).
16. Leadbeater, M., Winiecki, T., Samuels, D. C., Barenghi, C. F. & Adams, C. S. Sound emission due to superfluid vortex reconnections. *Phys. Rev. Lett.* **86**, 1410–1413 (2001).
17. Ruostekoski, J. & Dutton, Z. Engineering vortex rings and systems for controlled studies of vortex interactions in Bose-Einstein condensates. *Phys. Rev. A* **72**, 063626 (2005).
18. Villois, A., Proment, D. & Krstulovic, G. Irreversible dynamics of vortex reconnections in quantum fluids. *Phys. Rev. Lett.* **125**, 164501 (2020).
19. Kivotides, D., Vassilicos, J. C., Samuels, D. C. & Barenghi, C. F. Kelvin waves cascade in superfluid turbulence. *Phys. Rev. Lett.* **86**, 3080–3083 (2001).
20. Kozik, E. & Svistunov, B. Kelvin-wave cascade and decay of superfluid turbulence. *Phys. Rev. Lett.* **92**, 035301 (2004).
21. L'vov, V. S. & Nazarenko, S. Spectrum of Kelvin-wave turbulence in superfluids. *JETP Lett.* **91**, 428–434 (2010).
22. Popov, V. N. Quantum vortices and phase transitions in Bose systems. *Sov. Phys. JETP* **37**, 341–345 (1973).
23. Ambegaokar, V., Halperin, B. I., Nelson, D. R. & Siggia, E. D. Dynamics of superfluid films. *Phys. Rev. B* **21**, 1806–1826 (1980).
24. Arovas, D. P. & Freire, J. Dynamical vortices in superfluid films. *Phys. Rev. B* **55**, 1068–1080 (1997).
25. Bradley, D. I. et al. Direct measurement of the energy dissipated by quantum turbulence. *Nat. Phys.* **7**, 473–476 (2011).
26. Fonda, E., Meichle, D. P., Ouellette, N. T., Hormoz, S. & Lathrop, D. P. Direct observation of Kelvin waves excited by quantized vortex reconnection. *Proc. Natl Acad. Sci. USA* **111**, 4707–4710 (2014).
27. Walmsley, P., Zmееv, D., Pakpour, F. & Golov, A. Dynamics of quantum turbulence of different spectra. *Proc. Natl Acad. Sci. USA* **111**, 4691–4698 (2014).
28. Caroli, C., De Gennes, P. & Matricon, J. Bound Fermion states on a vortex line in a type II superconductor. *Phys. Lett.* **9**, 307–309 (1964).
29. Kopnin, N. B. & Salomaa, M. M. Mutual friction in superfluid  $^3\text{He}$ : effects of bound states in the vortex core. *Phys. Rev. B* **44**, 9667–9677 (1991).
30. Nygaard, N., Bruun, G. M., Clark, C. W. & Feder, D. L. Microscopic structure of a vortex line in a dilute superfluid Fermi gas. *Phys. Rev. Lett.* **90**, 210402 (2003).
31. Sensarma, R., Randeria, M. & Ho, T.-L. Vortices in superfluid Fermi gases through the BEC to BCS crossover. *Phys. Rev. Lett.* **96**, 090403 (2006).
32. Silaev, M. A. Universal mechanism of dissipation in Fermi superfluids at ultralow temperatures. *Phys. Rev. Lett.* **108**, 045303 (2012).
33. Kwon, W. J., Moon, G., Choi, J.-Y., Seo, S. W. & Shin, Y.-I. Relaxation of superfluid turbulence in highly oblate Bose-Einstein condensates. *Phys. Rev. A* **90**, 063627 (2014).
34. Johnstone, S. P. et al. Evolution of large-scale flow from turbulence in a two-dimensional superfluid. *Science* **364**, 1267–1271 (2019).
35. Liu, X.-P. et al. Universal dynamical scaling of quasi-two-dimensional vortices in a strongly interacting fermionic superfluid. *Phys. Rev. Lett.* **126**, 185302 (2021).
36. Rooney, S. J., Blakie, P. B., Anderson, B. P. & Bradley, A. S. Suppression of Kelvin-induced decay of quantized vortices in oblate Bose-Einstein condensates. *Phys. Rev. A* **84**, 023637 (2011).
37. Neely, T. W., Samson, E. C., Bradley, A. S., Davis, M. J. & Anderson, B. P. Observation of vortex dipoles in an oblate Bose-Einstein condensate. *Phys. Rev. Lett.* **104**, 160401 (2010).
38. Park, J. W., Ko, B. & Shin, Y. Critical vortex shedding in a strongly interacting fermionic superfluid. *Phys. Rev. Lett.* **121**, 225301 (2018).
39. Samson, E. C., Wilson, K. E., Newman, Z. L. & Anderson, B. P. Deterministic creation, pinning, and manipulation of quantized vortices in a Bose-Einstein condensate. *Phys. Rev. A* **93**, 023603 (2016).
40. Donnelly, R. J. *Quantized Vortices in Helium II* (Cambridge Univ. Press, 1991).
41. Parker, N. G. Numerical Studies of Vortices and Dark Solitons in Atomic Bose-Einstein Condensates. PhD thesis, Univ. Durham (2004).
42. Bulgac, A. & Yu, Y. Vortex state in a strongly coupled dilute atomic fermionic superfluid. *Phys. Rev. Lett.* **91**, 190404 (2003).
43. Chien, C.-C., He, Y., Chen, Q. & Levin, K. Ground-state description of a single vortex in an atomic Fermi gas: from BCS to Bose-Einstein condensation. *Phys. Rev. A* **73**, 041603 (2006).
44. Simonucci, S., Pieri, P. & Strinati, G. C. Temperature dependence of a vortex in a superfluid Fermi gas. *Phys. Rev. B* **87**, 214507 (2013).
45. Jones, C. A. and Roberts, P. H. Motions in a Bose condensate. IV. Axisymmetric solitary waves. *J. Phys. A* **15**, 2599–2619 (1982).
46. Jackson, B., Proukakis, N. P., Barenghi, C. F. & Zaremba, E. Finite-temperature vortex dynamics in Bose-Einstein condensates. *Phys. Rev. A* **79**, 053615 (2009).
47. Moon, G., Kwon, W. J., Lee, H. & Shin, Y.-I. Thermal friction on quantum vortices in a Bose-Einstein condensate. *Phys. Rev. A* **92**, 051601 (2015).
48. Wittmer, P., Schmied, C.-M., Gasenzer, T. & Ewerz, C. Vortex motion quantifies strong dissipation in a holographic superfluid. *Phys. Rev. Lett.* **127**, 101601 (2021).
49. Aioi, T., Kadokura, T., Kishimoto, T. & Saito, H. Controlled generation and manipulation of vortex dipoles in a Bose-Einstein condensate. *Phys. Rev. X* **1**, 021003 (2011).
50. Stagg, G. W., Allen, A. J., Parker, N. G. & Barenghi, C. F. Generation and decay of two-dimensional quantum turbulence in a trapped Bose-Einstein condensate. *Phys. Rev. A* **91**, 013612 (2015).
51. Groszek, A. J., Simula, T. P., Paganin, D. M. & Helmerson, K. Onsager vortex formation in Bose-Einstein condensates in two-dimensional power-law traps. *Phys. Rev. A* **93**, 043614 (2016).
52. Baggaley, A. W. & Barenghi, C. F. Decay of homogeneous two-dimensional quantum turbulence. *Phys. Rev. A* **97**, 033601 (2018).
53. Cidrim, A., dos Santos, F. E. A., Galantucci, L., Bagnato, V. S. & Barenghi, C. F. Controlled polarization of two-dimensional quantum turbulence in atomic Bose-Einstein condensates. *Phys. Rev. A* **93**, 033651 (2016).
54. Karl, M. & Gasenzer, T. Strongly anomalous non-thermal fixed point in a quenched two-dimensional Bose gas. *New J. Phys.* **19**, 093014 (2017).
55. Yang, G., Zhang, S. & Han, W. Oblique collisions and catching-up phenomena of vortex dipoles in a uniform Bose-Einstein condensate. *Phys. Scr.* **94**, 075006 (2019).
56. Tylutki, M. & Wlazlowski, G. Universal aspects of vortex reconnections across the BCS-BEC crossover. *Phys. Rev. A* **103**, L051302 (2021).
57. Reeves, M. T., Billam, T. P., Anderson, B. P. & Bradley, A. S. Inverse energy cascade in forced two-dimensional quantum turbulence. *Phys. Rev. Lett.* **110**, 104501 (2013).
58. White, A. C., Anderson, B. P. & Bagnato, V. S. Vortices and turbulence in trapped atomic condensates. *Proc. Natl Acad. Sci. USA* **111**, 4719–4726 (2014).
59. Simula, T., Davis, M. J. & Helmerson, K. Emergence of order from turbulence in an isolated planar superfluid. *Phys. Rev. Lett.* **113**, 165302 (2014).
60. Kwon, W. J., Kim, J. H., Seo, S. W. & Shin, Y. Observation of von Kármán vortex street in an atomic superfluid gas. *Phys. Rev. Lett.* **117**, 245301 (2016).
61. Seo, S. W., Ko, B., Kim, J. H. & Shin, Y. Observation of vortex-antivortex pairing in decaying 2D turbulence of a superfluid gas. *Sci. Rep.* **7**, 4587 (2017).
62. Gauthier, G. et al. Giant vortex clusters in a two-dimensional quantum fluid. *Science* **364**, 1264–1267 (2019).

**Publisher's note** Springer Nature remains neutral with regard to jurisdictional claims in published maps and institutional affiliations.

© The Author(s), under exclusive licence to Springer Nature Limited 2021

## Methods

### Superfluid sample preparation

We initially prepare fermionic superfluid samples by evaporating a balanced two-component mixture of the lowest hyperfine spin states of  ${}^6\text{Li}$ ,  $|F=1/2, m_F = \pm 1/2\rangle$ , near their scattering Feshbach resonance at 832 G in an elongated, elliptic optical dipole trap, formed by horizontally crossing two infrared beams at a  $14^\circ$  angle<sup>63</sup>. A repulsive  $\text{TEM}_{01}$ -like optical potential at 532 nm with a short waist of about 13  $\mu\text{m}$  is then adiabatically ramped up before the end of the evaporation to provide strong vertical confinement. Next, a box-like potential is turned on to trap the resulting sample in a circular region of the  $x$ - $y$  plane (see “Deterministic vortex generation” and Extended Data Fig. 1). When both potentials have reached their final configuration, the infrared lasers forming the crossed dipole trap are adiabatically extinguished, completing the transfer into the final uniform pancake trap. As the box potential has a small dimension with respect to the elongated dipole trap employed for the evaporation, the high-entropy tails of the initial cloud are discarded during the transfer. Within the loading sequence, superfluids at  $1/k_F a \approx 2.5$  on the BEC and  $1/k_F a \approx -0.31$  on the BCS side of the crossover are produced by adiabatically sweeping the magnetic field from 832 G to 857 G and to 702 G, respectively. The Feshbach magnetic-field coils produce a harmonic confinement in the  $x$ - $y$  plane of about 8 Hz, which is partially cancelled by the repulsive  $\text{TEM}_{01}$ -like potential, yielding a small in-plane trapping frequency of about 2.5 Hz. This weak confinement has negligible effect on the sample over the 45  $\mu\text{m}$  radius of our box trap, resulting in an essentially homogeneous density<sup>64,65</sup> (Extended Data Fig. 1). We further confirm the good uniformity of the cloud by observing the orbiting motion of a long vortex dipole, shown in Extended Data Fig. 2.

We measure the temperature of the sample before ramping up the in-plane box potential, namely in the composite trap formed by the crossed infrared beams and the green  $\text{TEM}_{01}$ -like beam, by means of well-established techniques employed for degenerate gases in harmonic traps<sup>66</sup>. The temperature measured at unitarity equals  $T/T_F = 0.05(2)$ , where  $T_F$  is the Fermi temperature given by  $k_B T_F = (\hbar k_F)^2/2m$ . Here,  $k_F = (6\pi^2 n)^{1/3}$  is the Fermi wavevector, while  $k_B$ ,  $\hbar$  and  $m$  are the Boltzmann constant, reduced Planck constant and the atomic mass of  ${}^6\text{Li}$ , respectively. The condensate fraction of our BECs is measured to be  $\sim 90\%$ , from which the temperature is estimated. The reduced temperature  $T/T_F$  on the BCS side of the Feshbach resonance is expected to remain equal to that at unitarity, considering the adiabaticity of our slow magnetic-field sweep<sup>67</sup>. Given the moderate  $\sim 20\%$  change of  $T_c$  from unitarity to the BCS regime explored in our work<sup>68</sup>, the temperature of our system is well characterized by  $T = 0.3(1)T_c$  in all interaction regimes. The very small value of the mutual friction coefficient  $\alpha$  measured for a BEC superfluid further ensures that the transfer to the homogeneous box potential is adiabatic with no appreciable heating.

The typical final sample consists of about  $5 \times 10^4$  atoms per spin state in the box potential with vertical trap frequencies of 356(2) Hz, 503(15) Hz and 480(11) Hz in the BEC, unitary and BCS regimes, respectively. The resulting ratio between the Thomas–Fermi radius  $R_{\text{TF}}$  along the vertical  $z$  direction, and the characteristic length of the superfluid (characterizing also the size of a vortex core) determines the ratio between the vortex line length and core size. For the BEC, unitary and BCS regime, it equals  $R_{\text{TF}}/\xi \approx 5$ ,  $R_{\text{TF}}/k_F \approx 28$  and  $R_{\text{TF}}/k_F \approx 31$ , respectively. The characteristic lengths in the BEC, unitary and BCS regimes of our samples are  $\xi = 0.68(2) \mu\text{m}$ ,  $1/k_F = 0.27(1) \mu\text{m}$  and  $1/k_F = 0.29(1) \mu\text{m}$ , respectively.

### Deterministic vortex generation

Both the in-plane box potential and the chopstick technique for vortex creation are implemented using a digital micromirror device (DMD), illuminated with blue-detuned 532-nm light to sculpt arbitrary repulsive optical potentials on the atomic cloud through a high-resolution

imaging system<sup>66,69</sup>. We obtain dynamical control over the potential by displaying an appropriate sequence of images on the DMD, with a well-defined timing between each image set by external triggers. Among several ways to deterministically produce a vortex dipole in BECs<sup>37,39,49,70</sup>, the chopstick method<sup>39,71</sup> has the advantage of controlling each vortex, using two focused repulsive obstacles as effective tweezers for a vortex and an antivortex. By acting on the sequence of images displayed on the DMD, this method allows us to adjust the vortex dipole size, position and orientation at will.

To prepare a sequence of images corresponding to the moving obstacles, we cut out the obstacle profiles in the desired position from a DMD image that produces a homogeneous light profile (see the further details in ref. <sup>69</sup>). These images are superimposed with a pattern that creates a hard-wall circular box. When initially raising the DMD-created potential, the device displays the image of a circular box with an off-centred round obstacle inside. Subsequently, the single obstacle is split into two identical round obstacles, which are moved with a velocity set by the DMD picture-sequence frame rate. Each obstacle is maintained at constant potential height  $V_0$ , even at the initial stage, contrary to refs. <sup>39,71</sup>, where two independent beams of potential height  $V_0$  sum up to create an initial obstacle of height  $2V_0$ .

At the end of the movement, the obstacles are ramped down by decreasing the number of ON pixels on the DMD in correspondence of their final position. This effectively decreases their height  $V_0$ , as the finite resolution of the imaging system blurs the discreteness of the DMD image<sup>69</sup>. The DMD-based control of each obstacle is extended towards the creation of many dipoles as in Fig. 2 by employing many obstacle beams from the initial stage. In particular, dipole–dipole collisions are engineered by sweeping pairs of obstacles towards the centre of the cloud.

We observe that the chopstick protocol works universally well across the BEC–BCS crossover, provided that the speed of the obstacles is appropriately adjusted depending on the interaction strength, yielding a dipole generation probability close to 100%. Such efficiency does also not depend on the bosonic or fermionic nature of the superfluid, and it is nearly independent of the tuning angle  $\theta$  for  $10^\circ \lesssim \theta \lesssim 30^\circ$ . The shot-to-shot fluctuations of the size  $d_{12}$  of the generated dipoles are quantified by an uncertainty of approximately 1  $\mu\text{m}$ , corresponding to the standard deviation over more than 40 realizations. We attribute such uncertainty to the fact that the size  $\sigma = 1.3(1) \mu\text{m}$  of our obstacles exceeds the vortex core size, allowing a vortex and an antivortex to be located away from the centre of each obstacle. The chopsticks are optimally designed to be sufficiently small to ensure stable generation of a short dipole of a few  $\xi$ , but also sufficiently large to pin and drag each vortex. Correspondingly, we adopt a quite fast ramp-down time of 0.8 ms of the obstacles, which is necessary to prevent short dipoles from annihilating while obstacles are not yet completely extinguished. On the other hand, for larger dipoles shown in Extended Data Fig. 2, and doubly charged dipole generation shown in Fig. 2e, we employ larger obstacles with  $\sigma \approx 3.3 \mu\text{m}$  to obtain a more stable dragging and pinning at large  $\theta$ . We stress that the large obstacle size is indeed favourable to create doubly charged dipoles in our experiments, possibly due to the larger depletion provided by the obstacle to accommodate the larger core of a multiply charged vortex.

### Vortex imaging

In weakly interacting BECs, where the condensed fraction reaches unity at zero temperature, a vortex is signalled by a clear hole in the atomic density over a length scale around the healing length  $\xi$  of the condensate. Thus, in the BEC regime we detect vortices by simply employing 1-ms time-of-flight (TOF) imaging. However, when working in the strongly interacting regime, a vortex excitation does not produce a significant density depletion, as the condensed fraction monotonically decreases towards the BCS side of the resonance. To detect vortices here, we therefore perform a rapid sweep of the magnetic field towards the BEC side of the resonance<sup>8,72</sup>, by which the order parameter of fermion pairs

can be converted into a BEC of tightly bound molecules. In particular, at unitarity and in the BCS regime, after the hold time  $t$ , we linearly sweep the magnetic field to 735 G in 3 or 3.3 ms, respectively. The final part of this sweep takes place while the cloud expands in TOF for 1 ms.

Our high-resolution imaging system, whose numerical aperture  $NA \approx 0.5$  guarantees a submicrometre resolution ( $\sim 0.9 \mu\text{m}$ ) at the absorption imaging wavelength of 670 nm, allows also direct observation of vortices in situ in the BEC regime<sup>73</sup>. Extended Data Fig. 1b shows the in situ image of a vortex (inset) together with its integrated radial profile (main), obtained by averaging over about 10 experimental realizations. We extract the vortex core size by performing a Lorentzian fit of the measured radial profile, obtaining a width of  $0.87(6) \mu\text{m}$ . We compare this value with the expected width from a numerical simulation of the vortex profile imaged by our setup. For this, we convolve the approximate vortex core profile<sup>74</sup>  $\rho(r) \propto r/\sqrt{2\xi^2 + r^2}$  with the independently determined point spread function of our imaging system, well approximated by a Gaussian of  $1/e^2$  radius of  $0.7 \mu\text{m}$ . The simulated vortex profile has a Lorentzian width of  $0.93(1) \mu\text{m}$ , consistent with the experimental vortex core size. This demonstrates that our estimation of  $\xi$  based on the trapping parameters and the atom number is reliable. Despite the demonstrated capability to detect vortices in situ, we adhere to TOF imaging, which benefits from reduced shot-to-shot fluctuations of the vortex visibility.

### Data analysis

To detect the position of each vortex, we apply an automated sequence that first blurs the experimental absorption image, and then converts it into a binary image, where the density-depleted holes corresponding to vortices appear as particles<sup>33,75</sup>. We extract the position of each particle, and use it as the initial guess of a Gaussian fit of the original image to obtain the position of each corresponding vortex. When the automated protocol fails, we estimate the approximate position of each vortex manually, and use this as the initial guess for Gaussian fitting. In this way, we obtain the size of each vortex dipole which is averaged over many realizations (30–100) under the same experimental conditions.

Throughout this work, errors on the mean dipole number  $N_{\text{vd}}$  are evaluated by adding the standard error of the mean  $\sigma_N/\sqrt{Z}$  and a measurement uncertainty  $1/Z$ , where  $Z$  denotes the number of measurements, as a quadrature sum  $\sqrt{\sigma_N^2/Z + (1/Z)^2}$ . The inclusion of  $1/Z$  avoids a zero uncertainty for datasets with all equal outcomes. We note that the mismatch between the values of  $d_{\text{in}}$  in the  $\Gamma$  and  $P_a$  data of Fig. 3 arises from the different number of images considered for the estimation of the two quantities. In particular, whenever we measure a non-zero  $P_a$ , we exclude an equivalent fraction of data in our  $\Gamma$  extraction, corresponding to the lowest part of the distribution of  $d_{\text{in}}$ , to account for the fraction of annihilation events that are expected to occur for the shortest dipoles. Thus, to precisely measure  $\Gamma$  at very small  $d_{\text{in}}$  close to the annihilation condition, it would be desirable to monitor the collision dynamics in real time.

### DPV model

In the framework of the two-fluid model, a quantum vortex experiences a temperature-dependent mutual friction force proportional to the relative velocity between the vortex and the normal component<sup>12</sup>. A DPV model<sup>12,76,77</sup> is formulated in terms of two phenomenological mutual friction (dimensionless) coefficients  $\alpha$  and  $\alpha'$ , characterizing the longitudinal dissipative and transverse non-dissipative force, respectively. As a first approximation, we include only  $\alpha$  in the model as  $\alpha'$  is in general quite small<sup>4</sup>. Taking into account the stationary normal fluid in our system, the model is given by

$$\mathbf{v}_i = \mathbf{v}_i^0 - w_i \alpha \hat{\mathbf{z}} \times \mathbf{v}_i^0, \quad (1)$$

where  $\mathbf{v}_i$  is the resultant velocity of the  $i$ th vortex, and  $\mathbf{v}_i^0$  is the local superfluid velocity created by the other vortices at the position of the

$i$ th vortex. The integer  $w_i$  is the winding number (positive for anticlockwise flow), and  $\hat{\mathbf{z}}$  is the unit vector along the axial (vertical) direction. This model has been successfully employed for describing the dynamics of vortices in atomic BECs at finite temperature<sup>47,78–81</sup>. The velocity of a vortex dipole of size  $d$  equals  $v_d = \hbar/(Md)$ , which is valid for  $d$  as small as a few  $\xi$  (ref. <sup>41</sup>), where  $M = 2m$  is the bosonic (atom pair) mass of  $^6\text{Li}$ , as directly verified by the trajectory of single dipoles (Fig. 1e). By plugging this relation into equation (1), one can directly obtain the following analytic formula

$$d(0)^2 - d(t)^2 = 4\alpha\hbar t/M, \quad (2)$$

where  $d(t)$  is the size of the dipole at time  $t$ . Consequently, the vortex lifetime  $\tau$  is determined by

$$\tau = \frac{M}{4\alpha\hbar} (d(0)^2 - d_c^2), \quad (3)$$

where  $d_c$  denotes the critical length below which a vortex dipole self-annihilates. From these relations, we independently obtain  $\alpha$  from the two measurements of Fig. 1f, g, and further the critical dipole length  $d_c$  from Fig. 1f.

To decouple the thermal dissipation from the total vortex energy loss in head-on collisions of two dipoles, we numerically solve equation (1) inserting the  $\alpha$  coefficient measured in each regime (Fig. 1h). We let each dipole start their dynamics at a distance  $L = 13 \mu\text{m}$  from the centre of the cloud and evolve until the inter-dipole distance becomes  $2L$  after the collision. To satisfy the boundary condition of our circular geometry, we consider the motion of image vortices outside the cloud boundary. We plot the obtained  $\Gamma = d_{13}d_{24}/d_{12}d_{34}$  as dotted lines in Fig. 3.

### Numerical simulations

Real-time dynamical simulations of vortex dynamics in the molecular BEC regime at temperature  $T = 0$  are performed by numerically integrating the mean-field GPE

$$i\hbar \frac{\partial \Psi}{\partial t} = -\frac{\hbar^2}{2M} \nabla^2 \Psi + V\Psi + g|\Psi|^2 \Psi \quad (4)$$

for the complex macroscopic wavefunction  $\Psi(x, y, z, t)$ , where  $V$  is the external confining potential,  $g = 4\pi\hbar^2 a_{\text{M}}/M$  is the strength of the repulsive two-body interaction, and  $a_{\text{M}} = 0.6a \approx 53.3 \text{ nm}$  is the molecular scattering length. The external potential  $V$  is defined as  $V(r, z) = \frac{1}{2}M(\omega_r^2 r^2 + \omega_z^2 z^2) + 10\mu\theta(r/R_0 - 1)$ , where  $r = (x^2 + y^2)^{1/2}$ , and  $\{\omega_r, \omega_z\} = 2\pi\{2.5, 356\} \text{ Hz}$  are respectively the radial and axial trapping frequencies. Here,  $\theta(x)$  is the Heaviside step function,  $\mu = 920.6 \text{ h} \times \text{Hz}$  is the chemical potential, and  $R_0 = 45 \mu\text{m}$  is the radius of the cylindrical hard-box potential. We set the number of particles  $N = 4.8 \times 10^4$ , equal to the typical experimental value in BECs, leading to a healing length  $\xi = 0.68 \mu\text{m}$  at the centre of the sample.

Our numerical code employs second-order accurate finite-difference schemes to discretize spatial derivatives; the integration in time is performed via a fourth-order Runge–Kutta method. The grid spacings are homogeneous in the three Cartesian directions  $\Delta x = \Delta y = \Delta z = 0.4\xi = 0.27 \mu\text{m}$ , and the time step  $\Delta t = 3.6 \mu\text{s}$ . The number of grid points in the  $x$ ,  $y$  and  $z$  directions are  $\{N_x, N_y, N_z\} = \{384, 384, 80\}$ , leading to the computational box  $-52.82 \mu\text{m} \leq x \leq 52.82 \mu\text{m}$ ,  $-52.82 \mu\text{m} \leq y \leq 52.82 \mu\text{m}$  and  $-11.00 \mu\text{m} \leq z \leq 11.00 \mu\text{m}$ .

**Vortex imprinting.** We start the simulation with a Thomas–Fermi profile for the condensate density  $\rho \propto |\Psi|^2$ . To calculate the vortex-free ground state, we evolve the GPE in imaginary time until the relative decrease of energy  $\Delta E/E$  between two consecutive timesteps is smaller than the threshold  $\varepsilon = 10^{-5}$ . Once this ground state is reached, we numerically imprint the vortices. Vortex imprinting is accomplished by

imposing a Padé density profile<sup>82</sup> and a  $2\pi$  phase winding around the vortex axis. We then let the system evolve in imaginary time towards the lowest energy state employing the previously described energy convergence criterion. Once  $\Delta E/E < \varepsilon$ , we introduce a phenomenological dissipation in equation (4) for a very short initial transient to reduce the initial acoustic energy generated by the vortex imprinting procedure, and thereafter we start the evolution of the GPE in real time.

**Vortex tracking.** The algorithm for vortex tracking is based on the pseudo-vorticity unit vector

$$\hat{\omega} := \frac{\nabla\psi_{\text{R}} \times \nabla\psi_{\text{I}}}{|\nabla\psi_{\text{R}} \times \nabla\psi_{\text{I}}|}$$

which is tangent to the vortex line along its length<sup>83–85</sup>, where  $\psi = \psi_{\text{R}} + i\psi_{\text{I}}$ . We reconstruct each  $i$ th vortex ( $i = 1, \dots, 4$ ) with a spatial resolution  $\Delta\zeta = \Delta x/10$ . At each time  $t$ , each vortex is reconstructed as  $\mathbf{x}_i(t) = \{x_i(\zeta_j, t), y_i(\zeta_j, t), z_i(\zeta_j, t)\}_{j=1, \dots, n_p}$ , where  $\zeta_j = j\Delta\zeta$  is the discretized arc length, and  $n_p$  is the number of vortex discretization points. Then, to determine the trajectories on the  $x$ - $y$  plane, we average over the arc length obtaining  $\langle \mathbf{x}_i(t) \rangle = (\langle x_i(t) \rangle, \langle y_i(t) \rangle, 0)$ , as vortices are symmetrical with respect to the plane  $z = 0$ .

**The numerical extraction of the vortex dipole sizes.** Here we describe how we numerically extract the vortex dipole sizes before and after a collision (that is, the ratio  $\Gamma = d_{13}d_{24}/d_{12}d_{34}$ ). As there are tiny dipole size oscillations because of a small amount of sound energy remaining in the condensate, we obtain the dipole sizes by computing their average value in a certain time interval before and after the interaction period. To identify such interval, we first compute the temporal evolution of the vortex velocity direction  $\beta(t)$  defined (for example, for vortex 1, Fig. 3a) as follows

$$\beta(t) = \arctan\left(\frac{v_{1,y}(t)}{v_{1,x}(t)}\right), \quad (5)$$

where  $v_{1,x}(t) = d\langle x_1(t) \rangle/dt$  and  $v_{1,y}(t) = d\langle y_1(t) \rangle/dt$ . Second, we observe that, after an initial constant value, during the collision the angle  $\beta$  changes and, once the interaction between the four vortices ceases, it achieves its post-collision stationary value, indicating indeed a straight trajectory (Fig. 3a). For example, in the case of head-on collisions, we observe that before the collision  $\beta \simeq 0^\circ$ ; it then increases once the interaction with the other dipole starts until  $\beta \simeq 90^\circ$  as the interaction ceases (Extended Data Fig. 6). We thus define the interaction period as  $t \in [t_1, t_2]$ , with  $t_1$  being the last time instant where  $\beta \simeq 0^\circ$  and  $t_2$  being the first instant where  $\beta \simeq 90^\circ$ . The vortex dipole input size  $d_{\text{in}}$  is computed by averaging the vortex dipole size from the start of motion until  $t_1$ , while the vortex dipole output size  $d_{\text{out}}$  is calculated averaging the dipole sizes from  $t = t_2$  until the time where the inter-dipole distance is equal to  $2L$  (to mimic the experimental protocol). A similar protocol based on  $\beta$  is applied for  $120^\circ$  collisions. The shaded area in Fig. 3c represents the range between  $\Gamma + \Delta\Gamma$  and  $\Gamma - \Delta\Gamma$ , where  $\Delta\Gamma$  is a quadrature sum of the standard deviation of  $d_{\text{in}}$  and  $d_{\text{out}}$ .

**Dissipation of the incompressible kinetic energy.** The ‘classical’ kinetic energy of a BEC,  $E_k = \frac{1}{2}M\rho\mathbf{v} \cdot \mathbf{v}$ , without considering the quantum energy component  $(\hbar^2/2M)|\nabla \cdot \sqrt{\rho}\mathbf{v}|^2$ , can be decomposed into two terms: the incompressible part  $E_k^{\text{I}}$  and the compressible part  $E_k^{\text{C}}$ . The former includes the energy stemming from vortices, while the latter refers to the acoustic energy of sound waves:

$$E_k^{\text{I}} = \int \frac{1}{2}M \left[ (\sqrt{\rho}\mathbf{v})^{\text{I}} \right]^2 dr,$$

$$E_k^{\text{C}} = \int \frac{1}{2}M \left[ (\sqrt{\rho}\mathbf{v})^{\text{C}} \right]^2 dr,$$

where  $\nabla \cdot (\sqrt{\rho}\mathbf{v})^{\text{I}} = 0$  and  $\nabla \times (\sqrt{\rho}\mathbf{v})^{\text{C}} = 0$ , with the fields  $(\sqrt{\rho}\mathbf{v})^{\text{I}}$  and  $(\sqrt{\rho}\mathbf{v})^{\text{C}}$  calculated via the Helmholtz decomposition<sup>13,86–90</sup>. To quantify the amount of incompressible kinetic energy dissipated in sound waves during the collision of two vortex dipoles, we compute the increase of the compressible kinetic energy  $\Delta E_k^{\text{C}}$  defined as  $\Delta E_k^{\text{C}} = E_k^{\text{C},t_2} - E_k^{\text{C},t_1}$  (Extended Data Fig. 7). The dependence of  $\Delta E_k^{\text{C}}$  on the input vortex dipole size  $d_{\text{in}}$  is shown in Fig. 3c (inset). While in Fig. 3c the dependence of  $\Gamma$  on  $d_{\text{in}}$  is shown only for the cases of collisions without vortex annihilations, the inset includes  $\Delta E_k^{\text{C}}$  for smaller values of  $d_{\text{in}}$  where vortex annihilations could occur.

## Data availability

The data that support the figures within this paper are available from the corresponding author upon reasonable request.

63. Burchianti, A. et al. Connecting dissipation and phase slips in a Josephson junction between fermionic superfluids. *Phys. Rev. Lett.* **120**, 025302 (2018).
64. Mukherjee, B. et al. Homogeneous atomic Fermi gases. *Phys. Rev. Lett.* **118**, 123401 (2017).
65. Hueck, K. et al. Two-dimensional homogeneous Fermi gases. *Phys. Rev. Lett.* **120**, 060402 (2018).
66. Del Pace, G., Kwon, W. J., Zaccanti, M., Roati, G. & Scazza, F. Tunneling transport of unitary fermions across the superfluid transition. *Phys. Rev. Lett.* **126**, 055301 (2021).
67. Haussmann, R., Rantner, W., Cerrito, S. & Zwerger, W. Thermodynamics of the BCS-BEC crossover. *Phys. Rev. A* **75**, 023610 (2007).
68. Pini, M., Pieri, P., Jager, M., Denschlag, J. H. & Strinati, G. C. Pair correlations in the normal phase of an attractive Fermi gas. *New J. Phys.* **22**, 083008 (2020).
69. Kwon, W. J. et al. Strongly correlated superfluid order parameters from dc Josephson supercurrents. *Science* **369**, 84–88 (2020).
70. Kwon, W. J., Seo, S. W. & Shin, Y.-I. Periodic shedding of vortex dipoles from a moving penetrable obstacle in a Bose-Einstein condensate. *Phys. Rev. A* **92**, 033613 (2015).
71. Gertjerenken, B., Kevrekidis, P. G., Carretero-González, R. & Anderson, B. P. Generating and manipulating quantized vortices on-demand in a Bose-Einstein condensate: a numerical study. *Phys. Rev. A* **93**, 023604 (2016).
72. Ku, M. J. H. et al. Motion of a solitonic vortex in the BEC-BCS crossover. *Phys. Rev. Lett.* **113**, 065301 (2014).
73. Wilson, K. E., Newman, Z. L., Lowney, J. D. & Anderson, B. P. In situ imaging of vortices in Bose-Einstein condensates. *Phys. Rev. A* **91**, 023621 (2015).
74. Pethick, C. J. & Smith, H. *Bose-Einstein Condensation in Dilute Gases* (Cambridge Univ. Press, 2002).
75. Rakonjac, A. et al. Measuring the disorder of vortex lattices in a Bose-Einstein condensate. *Phys. Rev. A* **93**, 013607 (2016).
76. Iordanskii, S. V. Mutual friction force in a rotating Bose gas. *Sov. Phys. JETP* **22**, 160–167 (1966).
77. Schwarz, K. W. Three-dimensional vortex dynamics in superfluid <sup>4</sup>He: homogeneous superfluid turbulence. *Phys. Rev. B* **38**, 2398–2417 (1988).
78. Billam, T. P., Reeves, M. T. & Bradley, A. S. Spectral energy transport in two-dimensional quantum vortex dynamics. *Phys. Rev. A* **91**, 023615 (2015).
79. Kim, J. H., Kwon, W. J. & Shin, Y. Role of thermal friction in relaxation of turbulent Bose-Einstein condensates. *Phys. Rev. A* **94**, 033612 (2016).
80. Skaugen, A. & Angheluta, L. Origin of the inverse energy cascade in two-dimensional quantum turbulence. *Phys. Rev. E* **95**, 052144 (2017).
81. Stockdale, O. R. et al. Universal dynamics in the expansion of vortex clusters in a dissipative two-dimensional superfluid. *Phys. Rev. Res.* **2**, 033138 (2020).
82. Berloff, N. G. Padé approximations of solitary wave solutions of the Gross–Pitaevskii equation. *J. Phys. A* **37**, 11729 (2004).
83. Rorai, C., Skipper, J., Kerr, R. M. & Sreenivasan, K. R. Approach and separation of quantised vortices with balanced cores. *J. Fluid Mech.* **808**, 641–667 (2016).
84. Villosio, A., Proment, D. & Krstulovic, G. Universal and nonuniversal aspects of vortex reconnections in superfluids. *Phys. Rev. Fluids* **2**, 044701 (2017).
85. Galantucci, L., Baggaley, A. W., Parker, N. G. & Barenghi, C. F. Crossover from interaction to driven regimes in quantum vortex reconnections. *Proc. Natl Acad. Sci. USA* **116**, 12204–12211 (2019).
86. Numasato, R., Tsubota, M. & L’vov, V. S. Direct energy cascade in two-dimensional compressible quantum turbulence. *Phys. Rev. A* **81**, 063630 (2010).
87. Horng, T.-L., Hsueh, C.-H., Su, S.-W., Kao, Y.-M. & Gou, S.-C. Two-dimensional quantum turbulence in a nonuniform Bose-Einstein condensate. *Phys. Rev. A* **80**, 023618 (2009).
88. Griffin, A., Nazarenko, S. & Proment, D. Breaking of Josephson junction oscillations and onset of quantum turbulence in Bose-Einstein condensates. *J. Phys. A* **53**, 175701 (2020).
89. Khani, K. et al. Critical transport and vortex dynamics in a thin atomic Josephson junction. *Phys. Rev. Lett.* **124**, 045301 (2020).
90. Khani, K. et al. Dynamical phase diagram of ultracold Josephson junctions. *New J. Phys.* **22**, 123006 (2020).

**Acknowledgements** We thank C. F. Barenghi, A. Bulgac, P. Magierski, F. Marino, M. McNeil Forbes, N. P. Proukakis, G. Wlazłowski and the Quantum Gases group at LENS for fruitful discussions, and N. Cooper for careful reading of the manuscript. This work was supported by the European Research Council under grant agreement no. 307032, the EPSRC under grant no. EP/R005192/1, the Italian Ministry of University and Research under the PRIN2017 project CEnTraL, and the EU’s Horizon 2020 research and innovation programme under Marie Skłodowska-Curie grant agreement no. 843303.

---

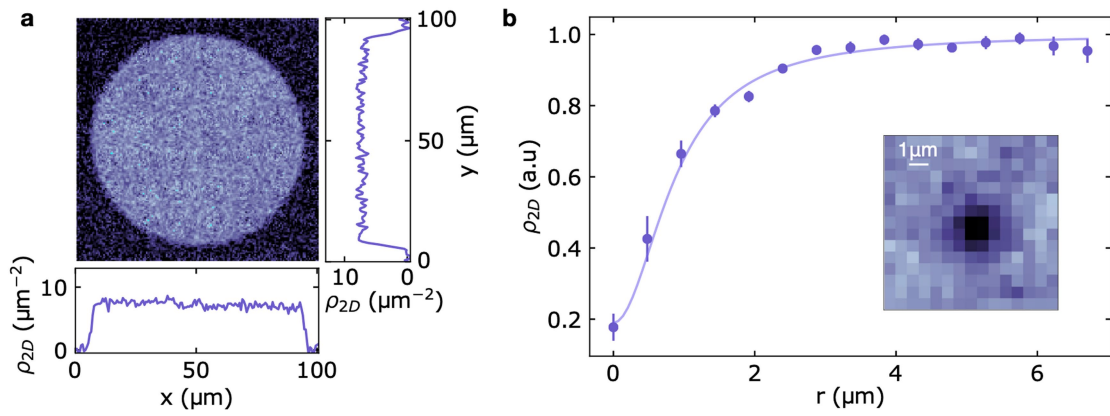
**Author contributions** W.J.K., G.D.P., F.S. and G.R. conceived the study. W.J.K., G.D.P., A.M.F. and F.S. performed the experiments. W.J.K. and G.D.P. analysed the experimental data. K.X. and L.G. carried out numerical simulations. All authors contributed to the interpretation of the results and to the writing of the manuscript.

**Competing interests** The authors declare no competing interests.

**Additional information**

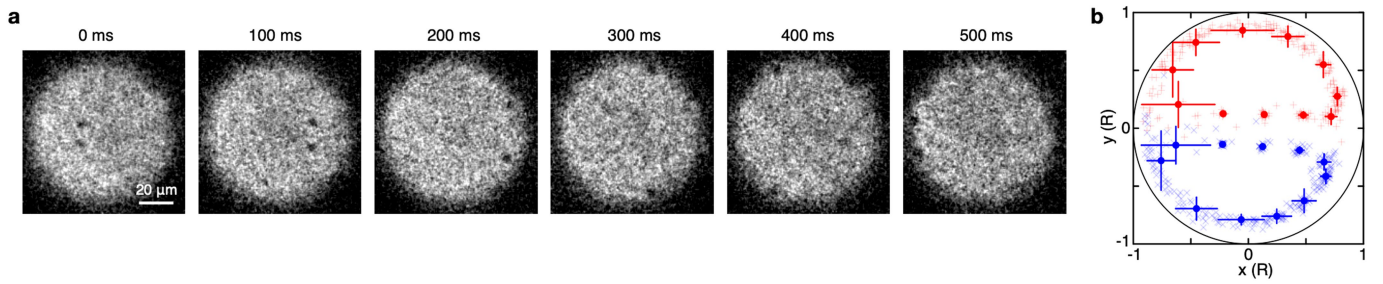
**Correspondence and** requests for materials should be addressed to W. J. Kwon.

**Peer review information** *Nature* thanks Ashton Bradley, Maren Mossman, Davide Proment and the other, anonymous, reviewer(s) for their contribution to the peer review of this work.



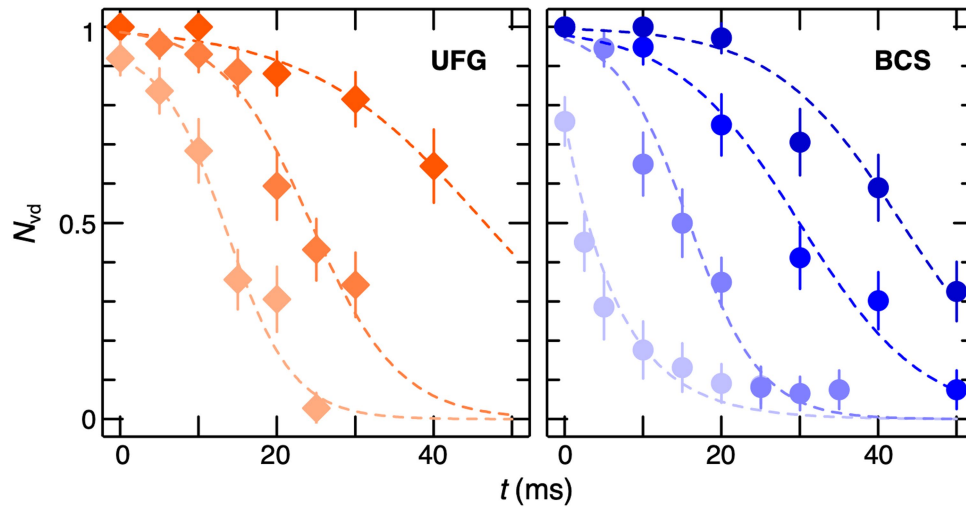
**Extended Data Fig. 1. | In situ profiles of homogeneous sample and an individual vortex.** **a**, In-plane density profile of a UFG sample from a single experimental shot, along with centred vertical and horizontal cuts averaged over 15 different experimental realizations. **b**, *In situ* vortex profile (inset) and its integrated radial profile (symbols) in a BEC sample. The image consists of

the average of 10 experimental realisations. The measured radial profile is fitted with a Lorentzian function (solid line), yielding a width of  $0.87(6) \mu\text{m}$ . This matches the expected value  $\xi \approx 0.68 \mu\text{m}$ , once the optical resolution of the imaging system is taken into account (see text).



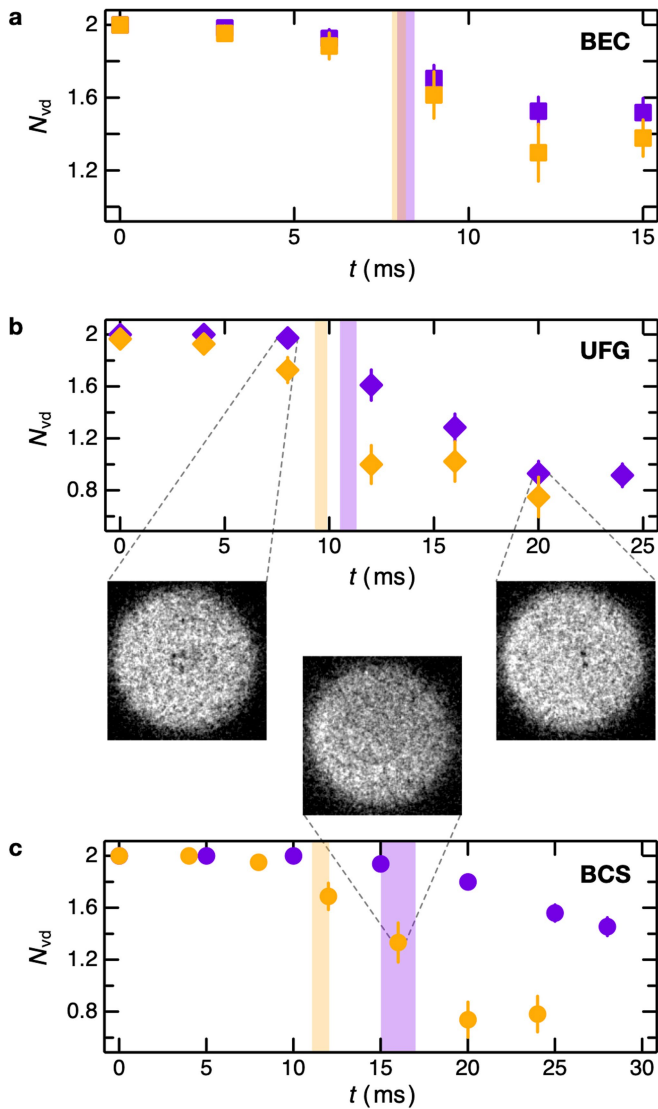
**Extended Data Fig. 2 | Orbiting motion of a large vortex dipole in UFGs.**  
**a**, A single dipole of  $d \approx 12 \mu\text{m}$  orbiting the homogeneous unitary Fermi gas of radius  $R = 45 \mu\text{m}$ . It rectilinearly crosses the cloud and then orbits it immediately adjacent to the boundary, in stark contrast to the observation of a vortex dipole shrinking and expanding during its propagation in a harmonic trap due to density inhomogeneity<sup>37</sup>. Each image is a single experimental shot.  
**b**, A trajectory obtained from the identical realisations of **a**. The hold time  $t$

varies from 0 to 500 ms with time intervals of 50 ms. The light red  $\times$  signs (blue  $+$ ) indicate single realisations of each vortex (antivortex) for the given  $t$ . The red (blue) circles represent the averaged positions of the vortices (antivortices) at the given  $t$ . Error bars indicate standard deviation over about 20 experimental measurements. After one orbit  $\sim 500 - 550$  ms, a survival probability of a vortex dipole decreases below 50%, probably due to interaction with the boundary.

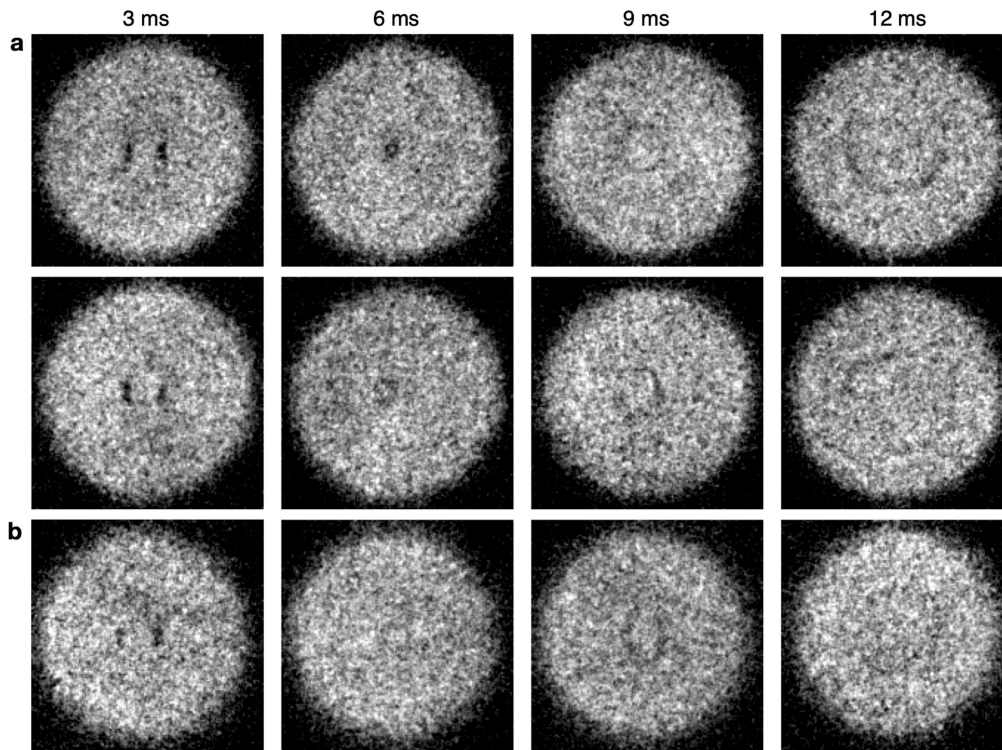


**Extended Data Fig. 3 | Decay of short vortex dipoles due to self-annihilation in UFG and BCS regimes.** The dipole half-life  $\tau$  for each initial  $d_{12}$ , i.e. the time required for  $N_{vd}$  to drop to half of its initial value, is determined by fitting  $N_{vd}(t)$  with a sigmoid function  $1/(1+e^{(t-\tau)/\gamma})$ , where the  $\gamma$  is used as the measurement

uncertainty. The only exception is the shortest dipole shown in the BCS regime, which is fitted with an exponential function. The initial  $d_{12}$  is controlled to range from 3.4 to 6  $\mu\text{m}$  (lighter colours denotes shorter dipoles). See also Fig. 1f. Error bars show the standard error of the mean over  $\sim 40$  experimental realisations.



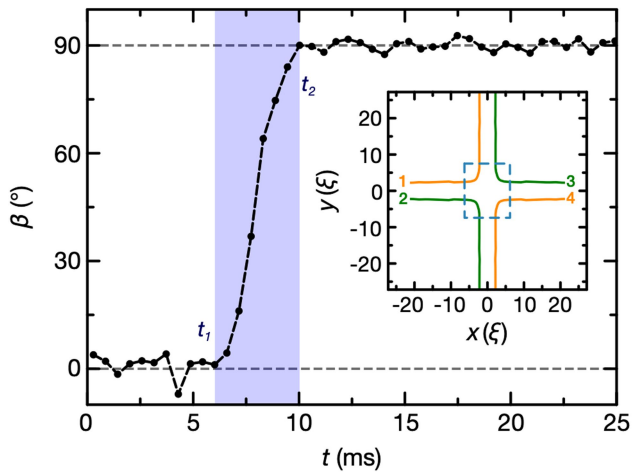
**Extended Data Fig. 4 | Time evolution of the number of vortex dipoles  $N_{vd}$  during dipole-dipole collisions.** Examples of  $N_{vd}(t)$  for head-on ( $120^\circ$ ) collisions are shown as orange (purple) symbols in (a) BEC, (b) UFG, and (c) BCS superfluids. Each data point consists of 40 – 60 same experimental realisations and the error bar indicates the standard error of the mean. Data sets are part of those for which  $P_a$  is shown in Fig. 3f-h of the main text, and specifically: (a)  $d_{in} \simeq 5\xi$ , (b)  $d_{in} \simeq 16/k_f$ , and (c)  $d_{in} \simeq 18/k_f$  (head-on) and  $d_{in} \simeq 24/k_f$  ( $120^\circ$ ). Shaded regions mark the time interval of vortex partner-exchange during a collision, estimated via DPV model imposing the condition  $0.9 < d_{13}(t)/d_{12}(t) < 1.1$ . The drop of  $N_{vd}(t)$  approximately matches this interval, confirming that the observed annihilations do not stem from single-dipole self-annihilations, but are an outcome of the collision dynamics. Experimental images show typical examples of a partial annihilation for a  $120^\circ$  collisions (b) and a rarely observed annihilation from head-on collisions in BCS superfluids (c). Images consist of single independent experimental shots.



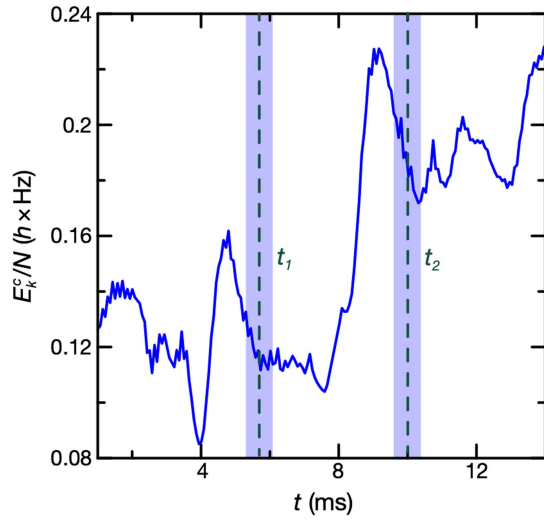
**Extended Data Fig. 5 | Vortex annihilation images for BECs and UFGs.**

Additional images display the clear emission of a density excitation following vortex annihilations in head-on collisions for **(a)** BECs and **(b)** UFGs. Two vortex dipoles collide horizontally as in Fig. 4 of the main text. The images in first and second rows of **(a)** are obtained independently with the same experimental parameters as in Fig. 4. By measuring the ring sizes of the density pulses observed in BECs ( $t = 9$  ms and  $t = 12$  ms), we find that the propagation speed of

the density pulse is around  $4.4(3)$  mm/s which coincides with the speed of sound evaluated from the mean density along the tight  $z$ -direction of the cloud. Annihilation images observed in UFGs are in general not as clear as in BECs, yet a number of images showing small-amplitude density waves propagating outwards are detected. Each shot is acquired in an independent experimental realisation.



**Extended Data Fig. 6 | Numerical criterion for selecting the vortex interaction period.** The temporal evolution of the direction  $\beta$  of the velocity of vortex 1 (cf. inset) is displayed for a head-on collision with  $d_{in} = 4.63\xi$ . The shaded area indicates the interaction interval  $[t_1, t_2]$  during which the dipole-dipole interaction takes place, with  $t_1$  being the last time instant where  $\beta \approx 0^\circ$  and  $t_2$  the first instant where  $\beta \approx 90^\circ$ . Inset: trajectories of the four vortices in the head-on collision. The dashed blue rectangle denotes the interaction region  $[t_1, t_2]$ .



**Extended Data Fig. 7 | Time evolution of the compressible kinetic energy  $E_k^c$  for the head-on collision and  $d_{in} = 4.43\xi$ .** The vertical dashed lines indicate times  $t_1$  and  $t_2$ , edges of the interaction interval. The increase of the compressible kinetic energy shown in Fig. 3c (inset) in the main paper is defined as  $\Delta E_k^c = E_k^{c,t_2} - E_k^{c,t_1}$ . More in detail, the initial  $E_k^{c,t_1}$  and the final  $E_k^{c,t_2}$  values of the compressible energy are extracted by computing an average value on a time interval of width  $\delta t$  centred at  $t_1$  and  $t_2$ , respectively. This is a characteristic time interval defined as  $\delta t = d_{in}/v_d$  corresponding to the shaded areas in the plot, where  $v_d = \hbar/Md_{in}$  is the vortex dipole velocity.